

Broadband TE Optical Isolators and Circulators in Silicon Photonics Through Ce:YIG Bonding

Paolo Pintus , *Member, IEEE*, Duanni Huang, Paul Adrian Morton , *Fellow, IEEE, Fellow, OSA*, Yuya Shoji , *Member, IEEE, Member, OSA*, Tetsuya Mizumoto , *Fellow, IEEE*, and John E. Bowers , *Fellow, IEEE, Fellow, OSA*

(Invited Paper)

Abstract—Optical isolators and circulators are fundamental building block in photonic integrated circuits to block undesired reflections and routing light according to a prescribed direction. In silicon photonics, heterogeneous integration of magneto-optic garnet bonded on a pre-patterned silicon layer has been demonstrated to be an effective solution for manufacturing optical isolators and circulators for TM polarized light. However, most integrated semiconductor lasers emit TE polarized light, which indicates the need to find a reliable solution for this polarization. In this paper, we demonstrated broadband optical isolators and circulators for TE polarized light based on heterogeneous bonding on the silicon photonics platform. To achieve this goal, an integrated adiabatic coupler and a broadband polarization rotator are designed and optimized. The nonreciprocal behavior is induced through an energy-efficient integrated electromagnet with a minimum power consumption of 3 mW. Two isolators/circulators are fabricated with small and large free spectral range, respectively. In the former case, an optical isolation ratio as large as 30 dB is measured at 1555 nm with an insertion loss of 18 dB, while for the broadband circulator, an optical isolation larger than 15 dB is guaranteed over more than 14 nm (1.75 THz) for all port combinations with an insertion loss between 14 and 18 dB at 1560 nm. Finally, it has been theoretically shown that the insertion loss can be reduced below 6 dB with design and fabrication improvements. To the best of the authors' knowledge, the proposed integrated TE optical circulator is the first experimental demonstration of this device in silicon photonics.

Index Terms—Integrated optical circulators, integrated optical isolators, integrated optoelectronics, Mach–Zehnder interferometers, magneto-optic devices.

Manuscript received October 13, 2018; revised January 18, 2019; accepted January 23, 2019. Date of publication January 31, 2019; date of current version March 27, 2019. This work was supported in part by the Air Force SBIR under Contract FA8650-16-C-1758 with Morton Photonics, in part by the “Center for Scientific Computing at UCSB,” and in part by NSF under Grant CNS-0960316. The work of D. Huang was supported by National Science Foundation Graduate Research Fellowship Program. (*Corresponding author: Paolo Pintus.*)

P. Pintus, D. Huang, and J. E. Bowers are with the Department of Electrical and Computer Engineering, University of California, Santa Barbara, CA 93106 USA (e-mail: ppintus@ece.ucsb.edu; duanni@ece.ucsb.edu; bowers@ece.ucsb.edu).

P. A. Morton is with Morton Photonics Inc., West Friendship, MD 21794 USA (e-mail: pmorton@mortonphotonics.com).

Y. Shoji and T. Mizumoto are with the Department of Electrical and Electronic Engineering, Tokyo Institute of Technology, Tokyo 152-8552, Japan (e-mail: shoji.y.ad@m.titech.ac.jp; tmizumot@pe.titech.ac.jp).

Color versions of one or more of the figures in this paper are available online at <http://ieeexplore.ieee.org>.

Digital Object Identifier 10.1109/JLT.2019.2896650

I. INTRODUCTION

SILICON photonics is now considered the most reliable and cost effective platform for very large-scale integration of photonic circuits operating at the second (~ 1310 nm) and the third telecom window (~ 1550 nm). Silicon is optically transparent at these wavelengths, which makes it an excellent material for low-loss passive optical components. Active components such as lasers and photodetectors have been effectively demonstrated by heterogeneous integration of III-V compound semiconductor and germanium on a pre-patterned silicon layer [1]. Despite the great achievements in manufacturing photonic integrated circuits (PIC) in silicon photonics, additional optical components that need to be efficiently integrated on the silicon-based platform to enable more complex and higher performance functionalities are optical isolators and circulators.

Optical isolators and circulators are unidirectional devices that allow the propagation of light in one direction and block the propagation in the opposite direction. They are used to reduce unintended optical feedback in lasers, allow serial integration by cascading multiple photonic components, and, in the case of optical circulator, asymmetrically routes light coming from different directions. Such a unique behavior is accomplished when the Lorenz reciprocity of the device is broken [2], which can be achieved three different ways: i) using spatial-temporal modulation (STM) of the refractive index [3]–[8], ii) exploiting nonlinear effects (NLE) [9]–[12], and iii) using magneto-optical (MO) materials [13]–[15]. The third solution has emerged as the most reliable in terms of circuit complexity, optical power efficiency, and wide isolation bandwidth. STM requires complex microwave driving circuits, while NLE suffers from low nonlinear conversion efficiency. Furthermore, optical devices based on STM and NLE operate with high performance only in a narrow bandwidth, since the refractive index modulation is wavelength sensitive, and the phase matching condition must be satisfied, respectively. On the other hand, the nonreciprocal effect in MO materials does not significantly change over a wide range of wavelengths when operating in the near and mid-infrared, allowing for a larger isolation bandwidth.

An optical wave that travels in a MO material is altered by the presence of an external magnetic field. The light may experience one or more nonreciprocal effects like the rotation of the polarization plane, the perturbation of the phase velocity,

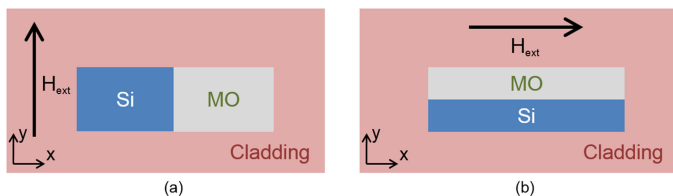


Fig. 1. Waveguide cross-section and external magnetic field that provides largest nonreciprocal phase shift for (a) TE and (b) TM modes.

or the variation of the propagation loss according to the direction of propagation and the orientation of the external magnetic field. When this field is perpendicular to the direction of propagation (Voigt configuration), forward and backward propagating waves exhibit different phase velocities. This is known as the nonreciprocal phase shift (NRPS) effect. Based on this effect, on-chip integrated optical isolators and circulators have been demonstrated in photonic crystals [16], [17], unbalanced Mach-Zehnder interferometers (MZI) [18]–[22], and microring resonators [23]–[28], where optical waves constructively interfere for a prescribed direction and destructively interfere for the opposite direction.

Because silicon is a reciprocal medium, several efforts have been made to integrate MO material on this platform. The typical MO material used at the telecom wavelengths is yttrium iron garnet (YIG), which is usually grown with cerium (Ce:YIG) or bismuth (Bi:YIG) atoms to increase the nonreciprocal effect. The explored approaches to integrate YIG on a silicon-platform are pulsed laser deposition [29], sputtering [30] and wafer bonding [25]. The first two approaches are appealing to realize monolithic integration of MO garnet on a silicon substrate because they provide conformal growth and sidewall coverage. However, the quality of the YIG grown on silicon, or amorphous silica, is far from that obtained by growing YIG on a gadolinium gallium garnet (GGG) substrate, which is the preferred native substrate due to the lattice matching.

In heterogeneous Ce:YIG/silicon waveguides, the NRPS is very sensitive to light polarization and the waveguide cross-section. Additionally, the magnetic field orientation must be properly arranged to maximize the phase shift between the forward and backward propagating direction. As explained in [31], for the TE mode, the optimum waveguide cross-section is horizontally discontinuous and the external magnetic field is perpendicular to the circuit plane; vice versa, for the TM mode, the waveguide is vertically discontinuous, and the magnetic field is in the plane of the waveguide – as shown in Fig. 1. The configuration of the optimal cross-section has important consequences for the fabrication and packaging of the device. While TM nonreciprocal waveguides can be fabricated in a straightforward manner by bonding MO garnet [32], TE nonreciprocal waveguides require deposition of the MO material in a lateral trench, on the side of the waveguide, which has not been effectively fabricated yet [33], [34]. Moreover, the intensity of the magnetic field needed to induce the nonreciprocal effect is significantly different for the in-plane and out-of-plane direction. For example, in Ce:YIG, the in-plane field (TM case) required to achieve the maximum NRPS is 50 Oe, while it is forty times stronger for the out-of-plane direction (TE case) [35]. As a result, TM

optical isolators and circulators are more easily assembled, and, as recently demonstrated, the in-plane saturation field can be efficiently generated using an integrated electromagnet [28], [36]. On the other hand, most semiconductor lasers emit TE polarized light, which indicates the need to develop TE optical isolators and circulators.

Since manufacturing TM optical isolators and circulators in silicon photonics holds the lead over the TE case, integrating polarization rotators with a TM isolator is, at the moment, the most effective solution for realizing the TE devices. Based on this approach, several solutions have been proposed. S. Ghosh *et al.* demonstrated MZI-based optical isolators that achieved an isolation ratio of 32 dB [37]. Although a large isolation is attained, the fabrication of the polarization rotator requires the deposition of 160 nm thick amorphous silicon over a 220 nm silicon layer, followed by a selective dry etch. Due to the complex geometries of the rotator structure, this approach is not straightforward to implement. Moreover, the largest NRPS is reached in a 220 nm silicon thick waveguide [32], so that the taller waveguide used in this work (i.e., 380 nm) implies a larger footprint for a prescribed NRPS (6 mm × 0.2 mm), resulting in a large insertion loss of 22 dB. A maximal isolation of 26.7 dB and excess loss of 26.2 dB for the TE mode at 1553 nm was demonstrated by Shoji *et al.*, implementing a planar polarization rotator with two asymmetric parallel waveguides [38]. The main advantage of this solution is that the patterning of the silicon layer requires a single lithography and etching step. On the other hand, this isolator still suffers from large losses and the implemented polarization rotator [39] is more sensitive to wavelength and fabrication variation than an adiabatic solution [40]. More recently, Yamaguchi *et al.* reduced the insertion loss down to 3.4 dB by replacing directional couplers with tapered mode converters [41]. Nevertheless, such mode converters limit the optical isolation to 16 dB because of a Fabry-Perrot resonance between the input and the output of the multi-mode interferometer junctions.

All the proposed solutions refer to an integrated optical isolator, while no TE optical circulator has been fabricated in silicon photonics. A TE optical circulator is more challenging to fabricate, and, in an MZI-based circulator, the 50:50 couplers must be perfectly balanced to provide the same isolation ratio at all ports. In this work, we demonstrate, for the first time, to the best of our knowledge, a broadband TE integrated optical circulator in silicon photonics. Although the results are mainly focused on the circulator, the same components can be effectively employed as a TE isolator by using only two ports, as described in [20], [21].

The device is fabricated by bonding Ce:YIG on a pre-patterned silicon-on-insulator (SOI) wafer. To operate for TE polarized light, a broadband integrated polarization rotator is designed and fabricated. The magnetic field is generated through two independent integrated electromagnets, which drive the nonreciprocal behavior in the Ce:YIG film. To reduce the drive current and power consumption in the electromagnet, the bonded GGG substrate is thinned down to a few microns. A multi-coil electromagnet is used, which drops the power consumption down to <1% of the value previously demonstrated for broadband TM optical isolators [20]. The final devices show

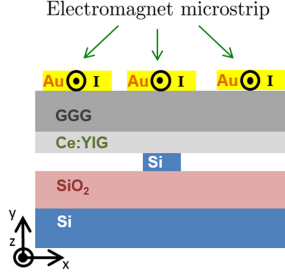


Fig. 2. Heterogeneous waveguide cross-section.

large isolation and wide isolation bandwidth. The integrated electromagnet provides an effective solution for device packaging, leading towards integration of nonreciprocal components in silicon photonics. Moreover, the thermal heating induced by the electromagnet can be gainfully used to tune the operating wavelength and compensate for fabrication deviations.

II. MZI-BASED ISOLATOR AND CIRCULATOR DESIGN

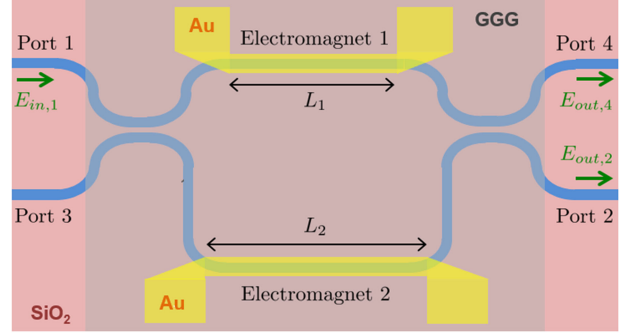
Broadband optical isolators and circulators can be effectively implemented using MZI geometry, where at least one of the two arms of the MZI is equipped with a nonreciprocal waveguide. In this section, the design of the sub-components for this device is described. After presenting the optimal nonreciprocal waveguide cross-section for the TM mode, the transfer function of the MZI-based circulator is derived with the definition of the design rules to achieve maximum optical isolation between two adjacent ports. Electromagnets are optimized to reduce the power consumption and TE-TM polarization rotators are presented in the last subsection.

A. Heterogeneous Waveguide Cross Section

The waveguide cross-section of the proposed device is schematically shown in Fig. 2. A high-quality Ce:YIG single crystal is grown on (Ca, Mg, Zr)-substituted GGG by using sputter epitaxy with a target of $\text{Ce}_1\text{Y}_2\text{Fe}_5\text{O}_{12}$. The MO die is bonded onto the pre-patterned SOI waveguides, and the GGG-substrate is then lapped to reduce the distance between the electromagnet and the Ce:YIG layer. Eventually, gold metal strips are deposited to create the electromagnets [36].

The cross-section is optimized to achieve the largest nonreciprocal shift at $\lambda_0 = 1550$ nm between TM forward and backward propagating modes; the thickness of the Ce:YIG layer is 400 nm, the thickness of the silicon (Si) layer is 220 nm, and the waveguide width is 600 nm. A 10 nm-thick oxide layer is also assumed between Ce:YIG and Si, which is a byproduct of the oxygen plasma assisted bonding process [28].

To compute the transfer function of the device, the effective index and the group index are calculated using the accurate finite element mode solver presented in [42]. All materials are low loss at $\lambda_0 = 1550$ nm, with the exception of the Ce:YIG which has a propagation loss of about 60 dB/cm, included in the mode analysis. When no current is injected in the electromagnet, the waveguide is reciprocal and the effective and group indices at $\lambda_0 = 1550$ nm are $n_{eff}(\lambda_0) = 2.18$ and $n_g(\lambda_0) = 3.2$, respectively. When the current is non-zero, the effective index in the

Fig. 3. Top view of an integrated Mach-Zehnder interferometer. In the case under study, the two arms have magneto-optic phase shifter with length L_1 and L_2 , respectively.

two directions is differentiated, i.e., $n_{eff}(\lambda_0) \pm \Delta n_M(\lambda_0)/2$, where the sign depends on the direction of the x-component of the magnetic field and so the direction of the current I, $\pm z$ in Fig. 2. The amplitude of Δn_M grows linearly with the current until it reaches its maximum value when the magnetization of the Ce:YIG is saturated. In this working condition, the Faraday rotation constant of the Ce:YIG reaches its peak, i.e., $\theta_F = -4800^\circ/\text{cm}$ [43], such that $\Delta n_{M,max} = 1.17 \cdot 10^{-3}$ at $\lambda_0 = 1550$ nm. On the contrary, the group index does not change significantly with the external magnetic field or with the direction. Since the electrical current induces local heating, the variation of the effective index and the degradation of the Faraday rotation constant, with respect to the temperature, is taken into account as shown in [28], [36]. Moreover, to include wavelength dispersion, the effective index is computed as

$$n_{eff}(\lambda) = n_{eff}(\lambda_0) \cdot \frac{\lambda}{\lambda_0} + n_g(\lambda_0) \cdot \left(1 - \frac{\lambda}{\lambda_0}\right) \quad (1)$$

while the simulated propagation loss is about 8.6 dB/cm in all operating conditions.

B. MZI Model and Design

Fig. 3 shows a push-pull MZI design, where each arm includes a heterogeneous waveguide, like the one described in the previous subsection. The two arms of the MZI are driven by integrated electromagnets with lengths L_1 and L_2 , to induce the nonreciprocal phase shift. The remaining lengths of the arms are L_{10} and L_{20} , respectively.

To compute the scattering matrix of a nonreciprocal MZI, the coupling matrix of the first coupler, the transfer function of the two arms, and the coupling matrix of the second coupler are cascaded. Following the port labelling shown in Fig. 3, the light is injected from Port 1 or Port 3, and collected at Port 2 and Port 4.

$$\begin{pmatrix} E_{out,4} \\ E_{out,2} \end{pmatrix} = \begin{pmatrix} t_2^* & -k_2 \\ k_2^* & t_2 \end{pmatrix} \cdot \begin{pmatrix} e^{j\phi_1^+} & 0 \\ 0 & e^{j\phi_2^+} \end{pmatrix} \cdot \begin{pmatrix} t_1 & k_1 \\ -k_1^* & t_1^* \end{pmatrix} \begin{pmatrix} E_{in,1} \\ E_{in,3} \end{pmatrix} \quad (2)$$

where k_1 (k_2) is the field cross-coupling coefficient and t_1 (t_2) is the field transmission coefficient of the first (second) coupler, while ϕ_1^+ and ϕ_2^+ are the phase shifts of arm 1 and arm 2,

respectively, when the light propagates from left to right in the figure. Analogous relations are derived when the light is sent from Port 2 or Port 4 and collected at Port 1 and Port 3

$$\begin{pmatrix} E_{out,1} \\ E_{out,3} \end{pmatrix} = \begin{pmatrix} t_1^* & -k_1 \\ k_1^* & t_1 \end{pmatrix} \cdot \begin{pmatrix} e^{j\phi_1^-} & 0 \\ 0 & e^{j\phi_2^-} \end{pmatrix} \cdot \begin{pmatrix} t_2 & k_2 \\ -k_2^* & t_2^* \end{pmatrix} \begin{pmatrix} E_{in,4} \\ E_{in,2} \end{pmatrix} \quad (3)$$

where ϕ_1^- and ϕ_2^- are the phase shifts of arm 1 and arm 2, respectively, when the light propagates in the backward direction. In Eqs. (2) and (3), the couplers are reciprocal and lossless (i.e., $|t_i|^2 + |k_i|^2 = 1$, for $i = 1, 2$).

As described in detail in the next section, the couplers are designed to be adiabatic and to split the power equally, i.e. $t_1 = t_2 = k_1 = k_2 = -j/\sqrt{2}$. For the light that propagates from left to right (or right to left) in Fig. 3, the two adiabatic couplers have opposite orientation, like in [44], which explains why the transfer matrices of coupler 1 and coupler 2 in Eq. (2) and Eq. (3) are formally one the inverse of the other. Adiabatic couplers are designed to operate over a broad bandwidth, and to achieve the same scattering coefficient between adjacent ports.

To derive the phase relation between the arms of the MZI, the propagation loss is neglected to a first approximation. Using the previous assumptions on the coupling coefficients, Eqs. (2) and (3) become

$$\begin{pmatrix} E_{out,4} \\ E_{out,2} \end{pmatrix} = e^{j\phi^+} \begin{pmatrix} \cos(\Delta\phi^+/2) & j \sin(\Delta\phi^+/2) \\ j \sin(\Delta\phi^+/2) & \cos(\Delta\phi^+/2) \end{pmatrix} \begin{pmatrix} E_{in,1} \\ E_{in,3} \end{pmatrix} \quad (4)$$

$$\begin{pmatrix} E_{out,1} \\ E_{out,3} \end{pmatrix} = e^{j\phi^-} \begin{pmatrix} \cos(\Delta\phi^-/2) & -j \sin(\Delta\phi^-/2) \\ -j \sin(\Delta\phi^-/2) & \cos(\Delta\phi^-/2) \end{pmatrix} \begin{pmatrix} E_{in,4} \\ E_{in,2} \end{pmatrix} \quad (5)$$

where

$$\phi^\sigma(\lambda) = [\phi_1^\sigma(\lambda) + \phi_2^\sigma(\lambda)]/2, \quad \sigma = +, - \quad (6.1)$$

$$\Delta\phi^\sigma(\lambda) = \phi_1^\sigma(\lambda) - \phi_2^\sigma(\lambda), \quad \sigma = +, - \quad (6.2)$$

Introducing the compact notation

$$s^\sigma = j e^{j\phi^\sigma} \sin(\Delta\phi^\sigma/2), \quad \sigma = +, - \quad (7.1)$$

$$c^\sigma = e^{j\phi^\sigma} \cos(\Delta\phi^\sigma/2), \quad \sigma = +, - \quad (7.2)$$

the scattering matrix is finally written as

$$\begin{pmatrix} E_{out,1} \\ E_{out,2} \\ E_{out,3} \\ E_{out,4} \end{pmatrix} = \begin{pmatrix} 0 & -s^- & 0 & c^- \\ s^+ & 0 & c^+ & 0 \\ 0 & c^- & 0 & -s^- \\ c^+ & 0 & s^+ & 0 \end{pmatrix} \begin{pmatrix} E_{in,1} \\ E_{in,2} \\ E_{in,3} \\ E_{in,4} \end{pmatrix} \quad (8)$$

which is akin to the one derived in [31] for a nonreciprocal ring-based optical circulator.

To achieve optical circulation according to the direction Port 1 → Port 2 → Port 3 → Port 4 → Port 1, the following relations must be satisfied

$$|c^+| = |s^-| = 0 \quad (9.1)$$

$$|c^-| = |s^+| = 1 \quad (9.2)$$

For the opposite circulating direction, i.e., Port 1 → Port 4 → Port 3 → Port 2 → Port 1, the following conditions must be fulfilled

$$|c^+| = |s^-| = 1 \quad (10.1)$$

$$|c^-| = |s^+| = 0 \quad (10.2)$$

The conditions stated in Eqs. (9) imply

$$\Delta\phi^- = 2m\pi \quad (11.1)$$

$$\Delta\phi^+ = \pi + 2n\pi \quad (11.2)$$

where n and m are integers. For the opposite circulating direction, the relation in Eqs. (11) are flipped, providing

$$\Delta\phi^- = \pi + 2m\pi \quad (12.1)$$

$$\Delta\phi^+ = 2n\pi \quad (12.2)$$

In both cases, the phase difference between $\Delta\phi^-$ and $\Delta\phi^+$ must be equal to an odd multiple of π , which means that the minimum phase shift to achieve optical isolation between the forward and the backward spectra is half of the free spectral range (FSR) of the MZI. For the device under investigation, the shift of the spectrum between the two operating conditions (e.g., forward and backward propagation) is equal to

$$\Delta\lambda = \lambda \cdot \frac{\Delta n_0 \cdot \Delta L_0 + \Delta n_2 \cdot L_2 - \Delta n_1 \cdot L_1}{n_{g,0} \cdot \Delta L_0 + n_{g,2} \cdot L_2 - n_{g,1} \cdot L_1} \quad (13)$$

where Δn_i , for $i = 0, 1, 2$, is the effective index variation of the reciprocal waveguide ($i = 0$) and the nonreciprocal waveguide under the two electromagnets ($i = 1, 2$); $n_{g,i}$, for $i = 0, 1, 2$, is the corresponding group index, and $\Delta L_0 = L_{20} - L_{10}$. Since the Ce:YIG is bonded on all the devices, the group indices in the three sections have very similar values $n_{g,0} \approx n_{g,1} \approx n_{g,2}$. Eq. (13) can also be written in terms of phase. When $\Delta\lambda$ is equal to a full FSR, which implies a phase variation equal to 2π , therefore $\Delta\phi = \Delta\lambda \cdot 2\pi/\text{FSR}$. The derivation of Eq. (13) is reported in the appendix.

When the currents in the two electromagnets have the same intensity but opposite directions, $\Delta n_0 = 0$ and $\Delta n_2 = -\Delta n_1 = \Delta n_M$, so that the spectrum shift due to the magneto-optic effect is

$$\Delta\lambda_M = \lambda \cdot \frac{\Delta n_M \cdot (L_2 + L_1)}{n_g \cdot (\Delta L_0 + L_2 - L_1)} \quad (14)$$

With the same current in the two electromagnets, the two arms of the MZI are locally heated and the spectrum is shifted due to the temperature increase

$$\Delta\lambda_T = \lambda \cdot \frac{\Delta n_T \cdot (L_2 - L_1)}{n_g \cdot (\Delta L_0 + L_2 - L_1)} \quad (15)$$

To maximize the optical isolation, the forward and backward spectra must be offset by half of the FSR. To minimize the thermo-optic effect, the lengths of the two electromagnets are made equal. The minimum length of the electromagnet is set from the condition $\Delta\lambda_M = \text{FSR}/2$, which is equivalent to Eq. (11) or Eq. (12) depending on the phase difference between $\Delta\phi^-$ and $\Delta\phi^+$. Recalling that $\text{FSR} = \lambda^2/(n_g \Delta L_0)$ [45], the

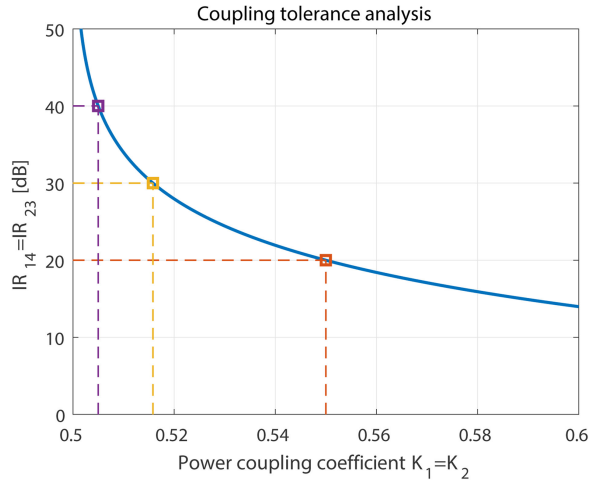


Fig. 4. Optical isolation ratio as a function of the power coupling coefficient of the directional couplers. By varying the splitting ratio of the power, the optical isolation between Port 1 and Port 4 (IR_{14}) and the one between Port 2 and Port 3 (IR_{23}) decrease. Same decreasing behavior is observed for $K_1, K_2 \leq 0.5$.

previous condition implies $L_1 = L_2 = \lambda / (4 \cdot \Delta n_{M,max})$ such that the minimum electromagnet length is $L_1 = L_2 = 342 \mu\text{m}$. Finally, the difference between the two arms lengths, ΔL_0 , can be independently chosen to set the FSR.

C. Adiabatic Power Splitter

To achieve large optical isolation between adjacent ports, the power splitter must equally split the optical power between the two arms. When this condition is not matched, the isolation decreases, and the performance of the device is limited. This particularly happens because the coupling coefficient changes with the wavelength or because of fabrication variability.

To quantify how the isolation ratio (IR) degrades with the coupling coefficient, the two couplers are assumed to be identical and to provide the same power splitting. As a result, the field coupling coefficients and the field transmission coefficients in Eqs. (2) and (3) are $|k_1| = |k_2| = \sqrt{K}$, and $|t_1| = |t_2| = \sqrt{1 - K}$, respectively, where K is the power coupling coefficient. When $K = 0.5$, the scattering matrix has the form in Eq. (8) and the isolation ratio is ideally infinite when Eq. (11) or Eq. (12) is satisfied. Vice versa, when the phase difference between $\Delta\phi^-$ and $\Delta\phi^+$ is still equal to $(2n + 1) \cdot \pi$ but $K \neq 0.5$, the isolation ratio between Port 1 and Port 4 (IR_{14}) and between Port 2 and Port 3 (IR_{23}) decrease as shown in Fig. 4, while the isolation ratio between Port 1 and Port 2 (IR_{12}) and between Port 3 and Port 4 (IR_{34}) remain infinite. The reason why IR_{12} and IR_{34} are still very large is that those parameters measure the isolation at the cross-ports, so that the light that travelled in the two arms is modulated equally by the two couplers and it results multiply by $\sqrt{K \cdot (1 - K)}$ for both arm 1 and arm 2. On the contrary, at the through port the light that propagates in one arm is tempered by K , while the light that travels in the other arm is reduced by $(1 - K)$, so condition (11) or (12) do not nullify the scattering coefficient. Since optical isolation is always very large at the MZI cross-port, compact directional couplers can be used instead for integrated isolators [20]. Vice versa, when optical circula-

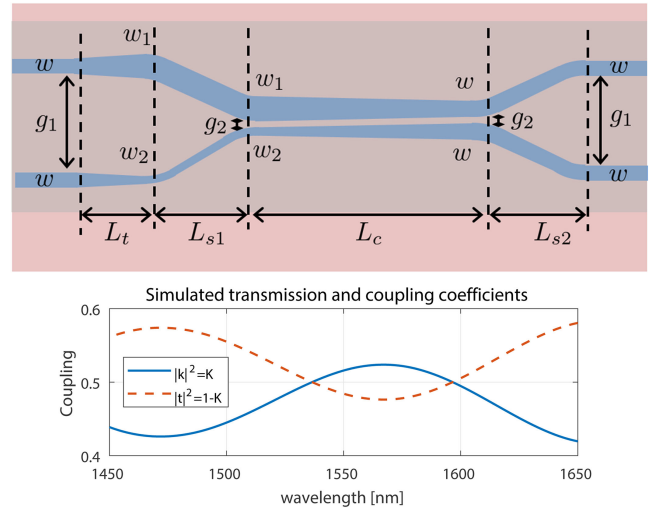


Fig. 5. Schematic layout of adiabatic directional coupler (top) and simulated field coupling coefficient (i.e., t) and field coupling coefficients (i.e., k) of the optimized adiabatic directional coupler (bottom).

TABLE I
ADIABATIC MODE-EVOLUTION-BASED COUPLER

Symbol	Description	Size
w	Waveguide width	600 nm
w_1	Waveguide width	700 nm
w_2	Waveguide width	500 nm
g_1	Waveguide distance	6 μm
g_2	Coupler distance	300 nm
L_t	Taper length	100 μm
L_{s1}	s-bend	100 μm
L_{s2}	s-bend	100 μm
L_c	Coupler length	200 μm

tor function is required, all ports must have the same behavior. To provide this, fabrication tolerant and wavelength insensitive adiabatic directional couplers are designed which call for a larger footprint.

For the purpose of this work, a mode-evolution-based adiabatic coupler proposed in [46] is implemented in the heterogeneous platform (Ce:YIG/Si). The schematic layout of the coupler is shown in Fig. 5 together with the numerical results, while the dimensions of the coupler are reported in Table I. From the analysis in Fig. 4, the above-mentioned optimized directional coupler will guarantee an extinction ratio larger than 20 dB over more than 100 nm. Indeed, $0.45 \leq K_1, K_2 \leq 0.55$ for $1504 \text{ nm} \leq \lambda \leq 1625 \text{ nm}$.

D. Integrated Electromagnet

This section is focused on optimization of the integrated electromagnet, which is fabricated by depositing a metal microstrip on the thinned GGG substrate. When current flows in the microstrip, a magnetic field is generated and the nonreciprocal effect is induced in the Ce:YIG [36]. Since the magnetic field decays with distance, the GGG substrate is mechanically thinned down to few microns after die bonding. The in-plane component of the magnetic field can be increased by using parallel microstrips or multi-coils, as proposed for micro-ring based

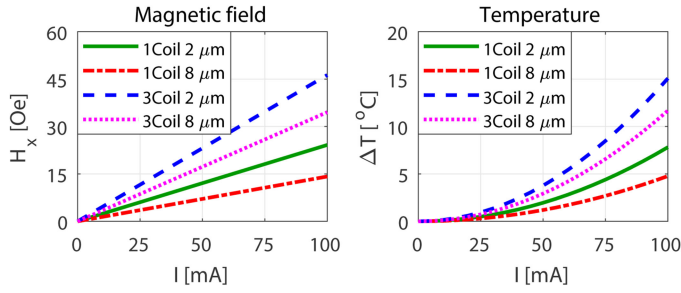


Fig. 6. The in-plane magnetic field at the Si/Ce:YIG interface (left) and the average temperature increment in the waveguide are computed with respect to the electrical current. Different substrate thicknesses ($2 \mu\text{m}$ and $8 \mu\text{m}$) are considered. The numerical results show field enhancement of three-coil electromagnet with respect to single coil solution.

optical isolators and circulators [28]. To work in a push-pull configuration, the currents in the two arms of the MZI are chosen to be in opposite directions.

The magnetic field and the temperature distribution is computed using COMSOL Multiphysics [47] assuming a 500 nm thick and $5 \mu\text{m}$ wide gold micro-strip, with a spacing of $3 \mu\text{m}$ in the case of multi-coils. The electrical and thermal constants used in the simulations are reported in the supplementary material of [27], while a more accurate estimation of the Ce:YIG magnetic permeability is extracted from magnetization measurement reported in [35]. As a result, the relative permeability is

$$\mu_{r,CeYIG} = \begin{pmatrix} 38.7 & 0 & 0 \\ 0 & 1.94 & 0 \\ 0 & 0 & 38.7 \end{pmatrix} \quad (16)$$

where the reference frame in Fig. 2 is considered.

The in-plane magnetic field at the Si/Ce:YIG interface and the average temperature increment in the waveguide are shown in Fig. 6 for $2 \mu\text{m}$ and $8 \mu\text{m}$ thick GGG substrates for the single and the three coil electromagnet cases. As expected, a larger in-plane field is produced by the thin GGG with a 3-coil electromagnet. In this case, 100 mA electrical current is needed to magnetically saturate the Ce:YIG, i.e., $H_x = 50 \text{ Oe}$, so that the largest nonreciprocal phase shift is produced (see Section II-A).

Since the magneto-optic effect decreases with the temperature induced by the electromagnet [48], and the magnetic field diminishes when the distance between the Ce:YIG and the electromagnet increases, L_1 and L_2 are chosen to be longer than the minimum values reported in Section II-B. A longer electromagnet is also beneficial for reducing the maximum current, consequently limiting electro-migration in the metal. Considering a more conservative length, the magneto-optic, $\Delta\lambda_M$, and thermal, $\Delta\lambda_T$, wavelength shifts are computed as a function of the electromagnet currents using Eq. (13), where the effective index is calculated with respect to the magnetic field and the thermal variation shown in Fig. 6.

The results are shown in Fig. 7 for different GGG thicknesses and electromagnets. As predicted in the previous section, when $|I_1| = |I_2|$ the thermal shift is very small, while the magneto-optic shift increases with increased current. By unbalancing the current in the two arms, a suitable thermal shift can

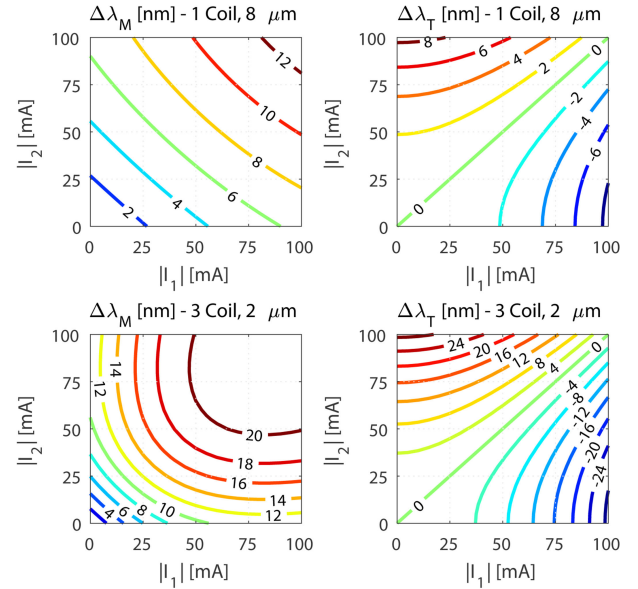


Fig. 7. Simulated magneto-optic and thermal wavelength shift of MZI circulators in the case $L_1 = L_2 = 1020 \mu\text{m}$ and $\Delta L_0 = 70 \mu\text{m}$. The cases with the lowest and largest magnetic field presented in Fig. 6 are considered. Similar results are achieved in other cases.

be used to trim the operating wavelength and compensate for fabrication deviations without compromising the nonreciprocal split between forward and backward spectra.

E. TE–TM Polarization Rotator

Since the waveguide cross-section in Fig. 2 maximizes the nonreciprocal phase shift for the TM mode, a TE→TM polarization rotator is placed at the MZI-port. The rotator consists of an adiabatic coupler followed by a linearly shaped taper. The former is used to couple the fundamental TE mode (TE₀) into the first higher TE mode (TE₁), as commonly used in mode-multiplexed systems. The latter converts the TE₁ mode into the fundamental TM mode (TM₀) through a mode hybridization effect [40]. This mode hybridization occurs at certain widths for which the TE₁ and TM₀ modes in the waveguide have similar refractive index. The waveguide geometry must be asymmetric as well, provided by the bonded Ce:YIG upper cladding in our device. The lengths of each section of the rotator are chosen such that the transition is fully adiabatic. The detailed dimensions of the polarization rotator can be found in [49].

III. EXPERIMENTAL RESULTS

In this section, the fabrication steps and the experimental characterization of the proposed device are presented. After characterizing the basic building blocks, i.e., the adiabatic coupler, the polarization rotator and the integrated electromagnet, the performance of the full device is evaluated in terms of optical isolation, insertion loss and isolation bandwidth.

A. Device Fabrication

A 220 nm -thick silicon-on-insulator (SOI) wafer is patterned using 248 nm deep ultra-violet lithography and dry etched using

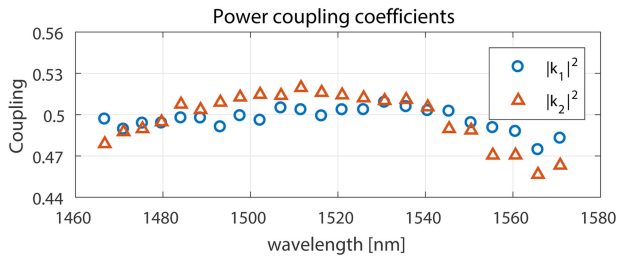


Fig. 8. Experimental characterization of the power coupling coefficients of the adiabatic couplers in a MZI.

a Bosch process. To prepare the sample for the bonding, the pre-patterned SOI wafer and the MO garnet are carefully cleaned and activated with O_2 plasma. The bonding with alignment is performed on a pick-and-place machine, and the process is completed by annealing the bonded sample at $200^\circ C$ for 6 hours under 3 MPa of pressure. A protective silica layer is sputtered on the final die before the lapping step, which is used to thin the GGG substrate. Finally, the metal stack is fabricated by evaporating 22 nm of titanium followed by 500 nm of gold [36].

Beyond the high quality of Ce:YIG separately grown on GGG, another benefit of the described bonding fabrication process is the compatibility with heterogeneous laser integration allowing for large volume manufacturing. For more detail about heterogeneous integration of optical isolators and circulators with lasers on silicon, the reader is referred to [49].

B. Device Characterization

The adiabatic coupler is characterized using the method proposed in [50]. Such a method allows for fully characterizing the power coupling coefficients of the adiabatic couplers from the extinction ratio of the MZI spectra in the case of small FSR. As shown in Fig. 8, the power coupling coefficients of the two adiabatic coupler in the MZI are very close to 50% over the wavelength range 1460 nm-1560 nm with a variation of less than 3%. This guarantees an IR larger than 25 dB in that wavelength range, as predicted from Fig. 4.

The experimental characterization of a 1.85 mm-long heterogeneous waveguide (i.e., Ce:YIG/Si) is shown in Fig. 9 in comparison with a $600\text{ nm} \times 220\text{ nm}$ silicon waveguide with a silica cladding. Assuming the scattering loss at the interfaces between the channel waveguide with a silica cladding and the Ce:YIG bonded waveguide is 0.6 dB/facet [36], the TM propagation loss is about 30 dB/cm at 1550 nm. This value is larger than the simulated one reported in Section II.A (i.e., 8.6 dB/cm) since the TM mode is located at the Ce:YIG/Si interface [32] and it suffers from the scattering loss, not included in the mode analysis. As shown in the following, this is the main cause of the large insertion loss of the isolator/circulator.

Figure 9 shows also the characterization of the polarization rotator that guarantees a polarization extinction ratio larger than 17 dB between the output TE and TM polarization. For this characterization, a TE-polarized light is injected in the polarization rotator and an external polarization beam splitter separates TE and TM components of the output signal. The insertion loss

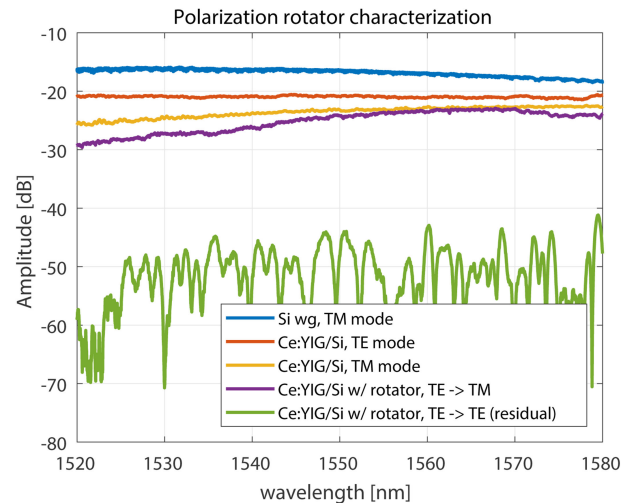


Fig. 9. Experimental characterization of the integrated broadband polarization rotator.



Fig. 10. Micrograph of integrated MZI optical circulators. Two electromagnetic configurations are shown in the figure, named 3-loop coil and 1-microstrip.

(IL_{rot}) is estimated by comparing those results with the TM mode loss in the heterogeneous Ce:YIG/Si waveguide.

Two different electromagnetic configurations are fabricated and investigated. The fabricated devices are shown in Fig. 10, where they are named “3-loop coil electromagnet” and “1-microstrip electromagnet”, respectively. The 3-loop coil electromagnet requires a single electrical source to control the nonreciprocal behavior of the two MZI arms. It provides a larger in-plane field (3 microstrips as shown in Fig. 6) and a longer nonreciprocal interaction compared to the two-distinct single microstrip cases. On the other hand, in the other device, the current of the two arms is independently controlled, holding the benefit of fine spectral tuning through thermal heating. For both configurations, the passive silicon MZI underneath is identical. To compare the experimental results with the theoretical model previously developed, note that the 3-loop coil electromagnet is equivalent to assuming that the two electromagnets fully cover the two arms and no reciprocal part is present, i.e., ΔL_0 is 0. As a result, for the device under investigation, the electromagnet lengths are $L_1 = 1450\ \mu\text{m}$ and $L_2 = 1520\ \mu\text{m}$ for the 3-loop coil electromagnet and $L_1 = L_2 = 1020\ \mu\text{m}$ for the 1-microstrip case, while ΔL_0 is 0 and $70\ \mu\text{m}$, respectively. In this way the FSR is equal to 10.7 nm in both configurations.

The nonreciprocal wavelength shift is measured by sweeping the current in the electromagnet, and the experimental results are shown in Fig. 11 for 4 MZI devices with different electromagnet configurations and GGG substrate thicknesses. The experimental (discrete markers) and theoretical (curves) results

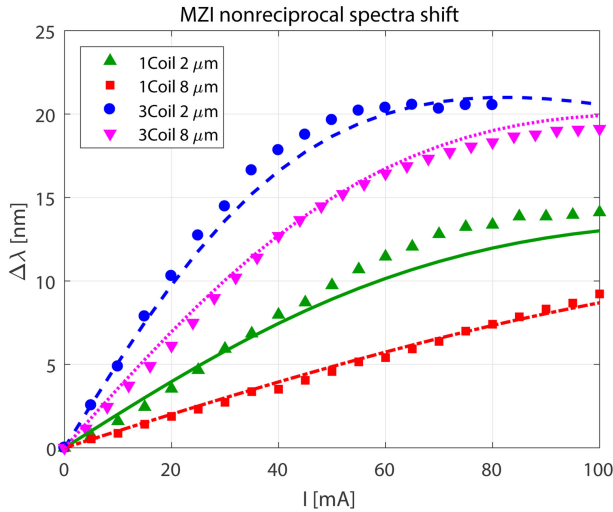


Fig. 11. Nonreciprocal wavelength shift in MZI-based optical circulator. Different electromagnets and GGG substrate thicknesses are investigated.

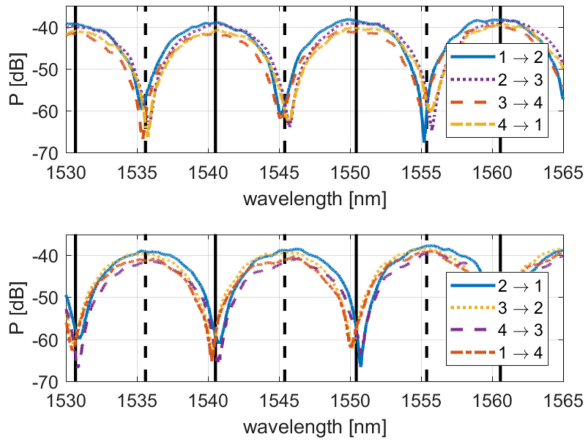


Fig. 12. Optical spectrum of MZI-based optical circulator in the C band, 1530 nm–1565 nm.

are plotted, showing an excellent agreement. In the device under investigation, $\Delta\lambda$ must be equal to 5.35 nm for optimal isolation ratio, meaning the nonreciprocal phase shift is equal to π . To meet this requirement, a current of 50 mA is needed in the 1-microstrip electromagnet with 8 μm thick GGG. Thinning the substrate down to 2 μm , results in a 50% lower driving current with a power consumption one fourth of the former case. A further current reduction down to 10 mA is achieved in the 3-loop coil electromagnet with longer magneto-optic interaction. In this case, the resistance of the electromagnet is roughly 30 Ω , meaning only 3 mW of electrical power is required. This is a significant improvement over previous MZI devices, which required 180 mA of current and 260 mW of power [20].

The optical behavior of the TE optical circulator is characterized in the C telecom band (1530 nm – 1565 nm). Considering the circulating direction Port 1 \rightarrow Port 2 \rightarrow Port 3 \rightarrow Port 4 \rightarrow Port 1, the optical spectra between two adjacent ports are shown on the top of Fig. 12, while the corresponding spectra in the opposite direction are reported on the bottom. The operating wavelengths in the direction Port 1 \rightarrow Port 2 \rightarrow Port 3 \rightarrow Port 4 \rightarrow Port 1 are highlighted with the continuous vertical

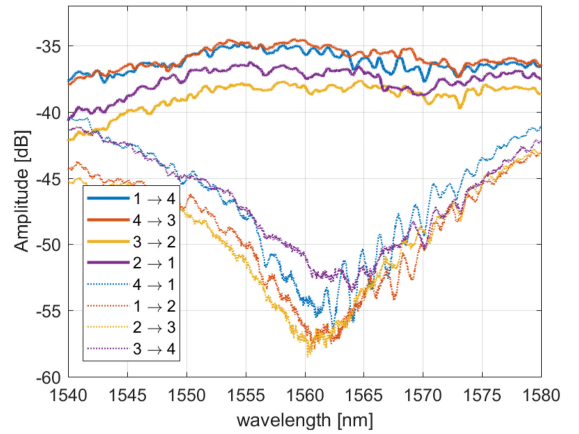


Fig. 13. Optical spectrum of MZI-based optical circulator 1530 nm–1565 nm.

line, while the dashed vertical line refers to the Port 1 \rightarrow Port 4 \rightarrow Port 3 \rightarrow Port 2 \rightarrow Port 1 operating wavelength. The isolation ratio computed between two adjacent ports reaches a maximum value of 30 dB near 1555 nm, while a minimum isolation larger than 18 dB between two adjacent ports is guaranteed across the C-band. The insertion loss of this device is between 18 dB and 21 dB and it is measured by comparing it to a straight silicon reference waveguide of the same dimensions, however, without the bonded Ce:YIG (not shown in Fig. 12).

Reducing the path difference between the two arms enlarges the FSR and allows for realizing an optical circulator that operates across a broader bandwidth. In the case of $\Delta L_0 = 1 \mu\text{m}$, the forward and backward optical spectra are shown in Fig. 13. The spectrum is centered at 1560 nm and an optical isolation of more than 18 dB is provided between each port pair. The IR slightly decreases with respect to the previous device because the mode conversion in the TE-TM polarization rotator has lower performance at different wavelengths and some residual TE is not fully converted. In this case, the insertion loss is between 14 dB and 18 dB when compared to a silicon reference waveguide at 1560 nm.

The isolation ratio for different isolation bandwidth (BW) is computed by using the following expression

$$IR(BW) = \frac{\int_{\lambda_0 - BW/2}^{\lambda_0 + BW/2} |S_{ij}(\lambda)|^2 d\lambda}{\int_{\lambda_0 - BW/2}^{\lambda_0 + BW/2} |S_{ji}(\lambda)|^2 d\lambda} \quad (17)$$

where S_{ij} and S_{ji} are the scattering coefficients in Eq. (8) between Port i and Port j , λ_0 is the central isolation wavelength or the wavelength where the minima of the backward spectra occurs. The results are shown in Fig. 14, where 15 dB of isolation ratio is guaranteed over more than 14 nm (1.75 THz).

The insertion loss (IL) is the main limitation of the current devices, however, its value can be significantly reduced. To understand how, all the contributions to the total insertion loss are analyzed. When a signal propagates from Port i to Port $i \pm 1$, where the index i is modulo 4, the light crosses two polarization rotators, two bonded facets and two adiabatic couplers. Since the two arms of the MZI have similar length and the power is equally split between them, this contribution is like the insertion

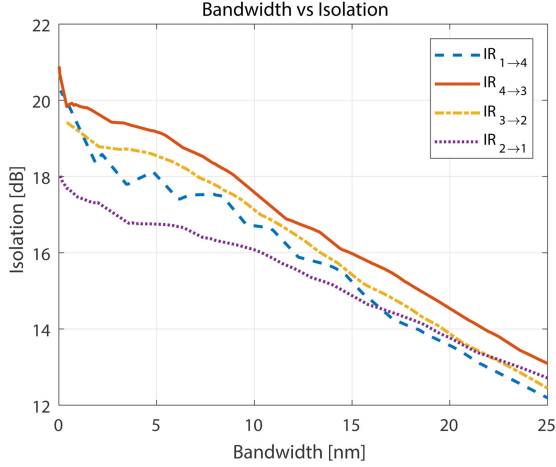


Fig. 14. Optical spectrum of MZI-based optical circulator 1530 nm–1565 nm.

loss of one arm only. As a result, IL can be written as

$$IL = 2 \cdot IL_{facet} + 2 \cdot IL_{rot} + 2 \cdot IL_{coup} + IL_{arm} \quad (18)$$

where $IL_{facet} = 0.6$ dB is due to the interfaces between the channel waveguide with a silica cladding and the Ce:YIG bonded waveguide [36], $IL_{rot} = 2.0$ dB is the insertion loss of the polarization rotator, $IL_{coup} = 2.2$ dB is the loss of the 50/50 adiabatic coupler and $IL_{arm} = 6.4$ dB is the loss in one arm of the MZI, respectively. As a result, the estimated IL is about 16 dB, which is close to the measured value of both devices. The variation of IL with respect to λ is due to two reasons. The propagation loss in the heterogeneous waveguide varies linearly between 44 dB/cm at 1520 nm and 16 dB/cm at 1580 nm, while the value of IL_{rot} ranges between 0.5 dB and 3 dB over the same wavelength spectrum. It is also worth noting that the insertion losses of the adiabatic coupler and the MZI arm are proportional to their lengths and to the propagation loss in the heterogeneous waveguide.

An effective way to reduce the IL is moving the polarization rotator inside the MZI like in [37] and reducing the length of the nonreciprocal phase shift to its minimum, i.e., $L_1 = L_2 = 342 \mu\text{m}$ as described in Section II.A. The implementation of this solution requires a precise bonding alignment or the development of an etching process for GGG and Ce:YIG similar to the one used for heterogeneous III-V on silicon [51]. Moreover, a larger current is needed to saturate the MO material. On the other hand, the benefits are a negligible insertion loss of the adiabatic coupler [46] and a loss as low as 1.0 dB for the MZI arm, resulting in a total insertion loss of about 6.0 dB. Moreover, optimization of the TE-TM polarization rotator can further reduce this value.

IV. CONCLUSION

In this work, integrated TE optical circulators in silicon photonics are experimentally demonstrated, for the first time, to the best of the authors' knowledge. Devices with different performance are fabricated using magneto-optic garnet bonding on a standard 220 nm-thick SOI wafer. Since bonding provides nonreciprocal phase shift for TM mode only, TE-TM polarization

rotators are designed at all ports to enable high performance optical circulators. The nonreciprocal effect is controlled by an integrated electromagnet, and an optical circulator is demonstrated for the C-band with an isolation ratio as large as 30 dB. A broadband optical circulator is fabricated for operation around 1560 nm, which guarantees optical isolation of more than 15 dB over 14 nm at all ports. Optimizing polarization rotator performance can further increase the optical isolation. Furthermore, power consumption needed to drive the integrated electromagnet has been successfully reduced to 3 mW, which is only 1.15% compared to 260 mW, which was previously demonstrated. Although this work is focused on optical circulators, the same devices can be employed as an integrated TE isolator using only two ports, providing an effective solution for integrating nonreciprocal devices in silicon photonics.

APPENDIX MZI SENSITIVITY

The sensitivity indicates the optical spectrum shift, $\Delta\lambda$, with respect to a reference operating condition due to an external perturbation. Several effects, such as magneto-optic or electro-optic effects, temperature variation and fabrication variability, can cause this shift. In this section, the sensitivity of an MZI is derived considering the unbalanced MZI shown in Fig. 2. Each arm of the MZI holds a magneto-optic phase shifter with lengths L_1 and L_2 , respectively. The remaining lengths of the arms are indicated by L_{10} and L_{20} , respectively.

The interference fringes of the spectrum are computed considering the constructive (or destructive) interference between the two arms. At the reference condition, the maxima of the output spectrum at the bar port are the wavelengths that solve the following equation

$$\beta_0(\lambda_1)L_{20} + \beta_2(\lambda_1)L_2 - \beta_0(\lambda_1)L_{10} - \beta_1(\lambda_1)L_1 = \pi + 2n\pi \quad (19)$$

where β_0 is the phase constant of the waveguide, while β_1 and β_2 are the phase constants of the magneto-optic waveguide in the two arms. An analogous relation can be written for the perturbed case

$$\tilde{\beta}_0(\lambda_2)L_{20} + \tilde{\beta}_2(\lambda_2)L_2 - \tilde{\beta}_0(\lambda_2)L_{10} - \tilde{\beta}_1(\lambda_2)L_1 = \pi + 2n\pi \quad (20)$$

where λ_2 is the interference wavelength, and the superscript tilde indicates the perturbed phase constants.

To compute the sensitivity, i.e., $\Delta\lambda = \lambda_1 - \lambda_2$, Eq. (19) and Eq. (20) are computed with respect to the central wavelength $\lambda = (\lambda_1 + \lambda_2)/2$, and the phase constant are replaced using the Taylor expansion series:

$$\beta_i \left(\lambda + \frac{\Delta\lambda}{2} \right) = \frac{2\pi}{\lambda} \left[n_i(\lambda) - n_{g,i}(\lambda) \frac{\Delta\lambda}{2\lambda} \right], \quad i = 0, 1, 2 \quad (21.1)$$

$$\tilde{\beta}_i \left(\lambda - \frac{\Delta\lambda}{2} \right) = \frac{2\pi}{\lambda} \left[\tilde{n}_i(\lambda) + \tilde{n}_{g,i}(\lambda) \frac{\Delta\lambda}{2\lambda} \right], \quad i = 0, 1, 2 \quad (21.2)$$

where n_i and $n_{g,i}$ are the effective index and the group index of the waveguide ($i = 0$) of the magneto-optic waveguide in arm 1 ($i = 1$) and arm 2 ($i = 2$), respectively. The superscript tilde in Eq. (21.2) indicates the perturbed effective index and the group index. Replacing Eq. (21.1) and Eq. (21.2) in Eq. (19) and Eq. (20), respectively, and computing the difference between the two equations, the following expression is derived

$$\Delta\lambda = \lambda \cdot \frac{\Delta n_0 \cdot \Delta L_0 + \Delta n_2 \cdot L_2 - \Delta n_1 \cdot L_1}{\bar{n}_{g,0} \cdot \Delta L_0 + \bar{n}_{g,2} \cdot L_2 - \bar{n}_{g,1} \cdot L_1} \quad (22)$$

where

$$\Delta L_0 = L_{20} - L_{10} \quad (23.1)$$

$$\Delta n_i = n_i(\lambda) - \tilde{n}_i(\lambda), \quad i = 0, 1, 2 \quad (23.2)$$

$$\bar{n}_{g,i} = [n_{g,i}(\lambda) + \tilde{n}_{g,i}(\lambda)]/2, \quad i = 0, 1, 2 \quad (23.3)$$

In Eqs. (23.1)–(23.3), ΔL_0 is the path difference between the two MZI arms, Δn_i , for $i = 0, 1, 2$, are the effective index variations between the reference and the perturbed cases and $n_{g,i}$, for $i = 0, 1, 2$, are the average group indices. For small $\Delta\lambda$, the average group indices in Eq. (23.3) can be approximated with n_g , since they do not change significantly. Eq. (22) is very similar to the one known for ring resonators $\Delta\lambda = \lambda \cdot \Delta n / n_g$ reported in [52].

ACKNOWLEDGMENT

The authors would like to thank J. Peters, L. Chang, M. Tran, and N. Collins for helpful discussions.

REFERENCES

- [1] L. Vivien and L. Pavesi, *Handbook of Silicon Photonics*. New York, NY, USA: Taylor & Francis, 2016.
- [2] D. Jalas *et al.*, “What is-and what is not-an optical isolator,” *Nature Photon.*, vol. 7, no. 8, pp. 579–582, 2013.
- [3] S. Bhandare, S. K. Ibrahim, D. Sandel, H. Zhang, F. Wüst, and R. Noé, “Novel nonmagnetic 30-dB traveling-wave single-sideband optical isolator integrated in III/V material,” *IEEE J. Sel. Topics Quantum Electron.*, vol. 11, no. 2, pp. 417–421, Mar./Apr. 2005.
- [4] C. R. Doerr, N. Dupuis, and L. Zhang, “Optical isolator using two tandem phase modulators,” *Opt. Lett.*, vol. 36, no. 21, pp. 4293–4295, 2011.
- [5] H. Lira, Z. Yu, S. Fan, and M. Lipson, “Electrically driven nonreciprocity induced by interband photonic transition on a silicon chip,” *Phys. Rev. Lett.*, vol. 109, no. 3, 2012, Art. No. 033901.
- [6] C. R. Doerr, L. Chen, and D. Vermeulen, “Silicon photonics broadband modulation-based isolator,” *Opt. Express*, vol. 22, no. 4, pp. 4493–4498, 2014.
- [7] J. N. Winn, S. Fan, J. D. Joannopoulos, and E. P. Ippen, “Interband transitions in photonic crystals,” *Phys. Rev. B*, vol. 59, no. 3, pp. 1551–1554, 1999.
- [8] Z. Yu and S. Fan, “Complete optical isolation created by indirect interband photonic transitions,” *Nature Photon.*, vol. 3, no. 2, pp. 91–94, 2009.
- [9] Y. Shi, Z. Yu, and S. Fan, “Limitations of nonlinear optical isolators due to dynamic reciprocity,” *Nature Photon.*, vol. 9, no. 6, pp. 388–392, 2015.
- [10] C. H. Dong, Z. Shen, C. L. Zou, Y. L. Zhang, W. Fu, and G. C. Guo, “Brillouin-scattering-induced transparency and non-reciprocal light storage,” *Nature Commun.*, vol. 6, pp. 1–6, 2015.
- [11] S. Hua, J. Wen, X. Jiang, Q. Hua, L. Jiang, and M. Xiao, “Demonstration of a chip-based optical isolator with parametric amplification,” *Nature Commun.*, vol. 7, pp. 1–6, 2016.
- [12] E. Krause, M. Renner, and H. Brinkmeyer, “Optical isolation in silicon waveguides based on nonreciprocal Raman amplification,” *Electron. Lett.*, vol. 44, no. 11, pp. 691–693, 2008.
- [13] H. Dötsch *et al.*, “Applications of magneto-optical waveguides in integrated optics: Review,” *J. Opt. Soc. Amer. B*, vol. 22, no. 1, pp. 240–253, 2005.
- [14] B. J. H. Stadler and T. Mizumoto, “Integrated magneto-optical materials and isolators: A review,” *IEEE Photon. J.*, vol. 6, no. 1, pp. 1–15, Feb. 2014.
- [15] T. Shoji and Y. Mizumoto, “Waveguide magneto-optical devices for photonics integrated circuits [Invited],” *Opt. Mater. Express*, vol. 8, no. 8, pp. 2387–2394, 2018.
- [16] Z. Wang and S. Fan, “Optical circulators in two-dimensional magneto-optical photonic crystals,” *Opt. Lett.*, vol. 30, no. 15, pp. 1989–1991, 2005.
- [17] W. Śmigaj, J. Romero-Vivas, B. Gralak, L. Magdenko, B. Dagens, and M. Vanwolleghem, “Magneto-optical circulator designed for operation in a uniform external magnetic field,” *Opt. Lett.*, vol. 35, no. 4, pp. 568–570, 2010.
- [18] J. Fujita, M. Levy, R. M. Osgood, L. Wilkens, and H. Dötsch, “Waveguide optical isolator based on Mach–Zehnder interferometer,” *Appl. Phys. Lett.*, vol. 76, no. 16, pp. 2158–2160, 2000.
- [19] Y. Shoji, T. Mizumoto, H. Yokoi, I. W. Hsieh, and R. M. Osgood, “Magneto-optical isolator with silicon waveguides fabricated by direct bonding,” *Appl. Phys. Lett.*, vol. 92, no. 7, 2008, Art. no. 071117.
- [20] D. Huang, P. Pintus, Y. Shoji, P. Morton, T. Mizumoto, and J. E. Bowers, “Integrated broadband Ce:YIG/Si Mach–Zehnder optical isolators with over 100 nm tuning range,” *Opt. Lett.*, vol. 42, no. 23, pp. 4901–4904, 2017.
- [21] E. Ishida *et al.*, “Amorphous-Si waveguide on a garnet magneto-optical isolator with a TE mode nonreciprocal phase shift,” *Opt. Express*, vol. 25, no. 1, pp. 452–462, 2017.
- [22] N. Sugimoto *et al.*, “Waveguide polarization-independent optical circulator,” *IEEE Photon. Technol. Lett.*, vol. 11, no. 3, pp. 355–357, Mar. 1999.
- [23] N. Kono, K. Kakihara, K. Saitoh, and M. Koshiba, “Nonreciprocal microresonators for the miniaturization of optical waveguide isolators,” *Opt. Express*, vol. 15, no. 12, pp. 7737–7751, 2007.
- [24] D. Jalas, A. Petrov, M. Krause, J. Hampe, and M. Eich, “Resonance splitting in gyrotropic ring resonators,” *Opt. Lett.*, vol. 35, no. 20, pp. 3438–3440, 2010.
- [25] M.-C. Tien, T. Mizumoto, P. Pintus, H. Kromer, and J. E. Bowers, “Silicon ring isolators with bonded nonreciprocal magneto-optic garnets,” *Opt. Express*, vol. 19, no. 12, pp. 11740–11745, 2011.
- [26] D. Jalas, A. Y. Petrov, and M. Eich, “Optical three-port circulators made with ring resonators,” *Opt. Lett.*, vol. 39, no. 6, pp. 1425–1428, 2014.
- [27] D. Huang *et al.*, “Dynamically reconfigurable integrated optical circulators,” *Optica*, vol. 4, no. 1, pp. 23–30, 2017.
- [28] P. Pintus, D. Huang, C. Zhang, Y. Shoji, T. Mizumoto, and J. E. Bowers, “Microring-based optical isolator and circulator with integrated electromagnet for silicon photonics,” *J. Lightw. Technol.*, vol. 35, no. 8, pp. 1429–1437, Apr. 2017.
- [29] L. Bi *et al.*, “On-chip optical isolation in monolithically integrated non-reciprocal optical resonators,” *Nature Photon.*, vol. 5, no. 12, pp. 758–762, 2011.
- [30] A. D. Block, P. Dulal, B. J. H. Stadler, and N. C. A. Seaton, “Growth parameters of fully crystallized YIG, Bi:YIG, and Ce:YIG films with high faraday rotations,” *IEEE Photon. J.*, vol. 6, no. 1, pp. 1–8, Feb. 2014.
- [31] P. Pintus, F. Di Pasquale, and J. E. Bowers, “Integrated TE and TM optical circulators on ultra-low-loss silicon nitride platform,” *Opt. Express*, vol. 21, no. 4, pp. 5041–5052, 2013.
- [32] P. Pintus, M. C. Tien, and J. E. Bowers, “Design of magneto-optical ring isolator on SOI based on the finite-element method,” *IEEE Photon. Technol. Lett.*, vol. 23, no. 22, pp. 1670–1672, Nov. 2011.
- [33] P. Pintus, F. Di Pasquale, and J. E. Bowers, “Design of transverse electric ring isolators for ultra-low-loss Si3N4 waveguides based on the finite element method,” *Opt. Lett.*, vol. 36, no. 23, pp. 4599–4601, 2011.
- [34] Y. Shoji *et al.*, “Magneto-optical isolator with silicon waveguides fabricated by direct bonding,” *Appl. Phys. Lett.*, vol. 92, no. 7, 2017, Art. no. 071117.
- [35] T. Goto, M. C. Onbaşlı, and C. A. Ross, “Magneto-optical properties of cerium substituted yttrium iron garnet films with reduced thermal budget for monolithic photonic integrated circuits,” *Opt. Express*, vol. 20, no. 27, pp. 28507–28517, 2012.
- [36] D. Huang, P. Pintus, C. Zhang, Y. Shoji, T. Mizumoto, and J. E. Bowers, “Electrically driven and thermally tunable integrated optical isolators for silicon photonics,” *IEEE J. Sel. Topics Quantum Electron.*, vol. 22, no. 6, Nov./Dec. 2016, Art. no. 4403408.
- [37] S. Ghosh, S. Keyvaninia, Y. Shirato, T. Mizumoto, G. Roelkens, and R. Baets, “Optical isolator for TE polarized light realized by adhesive bonding of Ce:YIG on silicon-on-insulator waveguide circuits,” *IEEE Photon. J.*, vol. 5, no. 3, Jun. 2013, Art. no. 6601108.

- [38] Y. Shoji, A. Fujie, T. Mizumoto, and I. Paper, "Silicon waveguide optical isolator operating for TE mode input light," *IEEE J. Sel. Topics Quantum Electron.*, vol. 22, no. 6, Nov./Dec. 2016, Art. no. 4403307.
- [39] L. Liu, Y. Ding, K. Yvind, and J. M. Hvam, "Efficient and compact TE-TM polarization converter built on silicon-on-insulator platform with a simple fabrication process," *Opt. Lett.*, vol. 36, no. 7, pp. 1059–1061, 2011.
- [40] D. Dai and J. E. Bowers, "Novel concept for ultracompact polarization splitter-rotator based on silicon nanowires," *Opt. Express*, vol. 19, no. 11, pp. 10940–10949, 2011.
- [41] R. Yamaguchi, Y. Shoji, and T. Mizumoto, "Low-loss waveguide optical isolator with tapered mode converter and magneto-optical phase shifter for TE mode input," *Opt. Express*, vol. 26, no. 16, pp. 21271–21278, 2018.
- [42] P. Pintus, "Accurate vectorial finite element mode solver for magneto-optic and anisotropic waveguides," *Opt. Express*, vol. 22, no. 13, pp. 15737–15756, 2014.
- [43] T. Shintaku, T. Uno, and M. Kobayashi, "Magneto-optic channel waveguides in Ce-substituted yttrium iron garnet," *J. Appl. Phys.*, vol. 74, no. 8, pp. 4877–4881, 1993.
- [44] M. A. Tran, C. Zhang, and J. E. Bowers, "A broadband optical switch based on adiabatic couplers," in *Proc. IEEE Photon. Conf.*, 2016, pp. 755–756.
- [45] L. Chrostowski and M. Hochberg, *Silicon Photonics Design*. Cambridge, U.K.: Cambridge Univ. Press, 2015.
- [46] Y. Wang *et al.*, "Polarization-independent mode-evolution-based coupler for the silicon-on-insulator platform," *IEEE Photon. J.*, vol. 10, no. 3, Jun. 2018, Art. no. 4900410.
- [47] COMSOL multiphysics. [Online]. Available: www.comsol.com
- [48] K. Furuya, T. Nemoto, K. Kato, Y. Shoji, and T. Mizumoto, "Athermal operation of a waveguide optical isolator based on canceling phase deviations in a Mach-Zehnder interferometer," *J. Lightw. Technol.*, vol. 34, no. 8, pp. 1699–1705, Apr. 2016.
- [49] D. Huang, P. Pintus, and J. E. Bowers, "Towards heterogeneous integration of optical isolators and circulators with lasers on silicon [Invited]," *Opt. Mater. Express*, vol. 8, no. 9, pp. 2471–2483, 2018.
- [50] M. A. Tran, T. Komljenovic, J. C. Hulme, M. L. Davenport, and J. E. Bowers, "A robust method for characterization of optical waveguides and couplers," *IEEE Photon. Technol. Lett.*, vol. 28, no. 14, pp. 1517–1520, Jul. 2016.
- [51] T. Komljenovic, D. Huang, P. Pintus, M. A. Tran, M. L. Davenport, and J. E. Bowers, "Photonic integrated circuits using heterogeneous integration on silicon," *Proc. IEEE*, vol. 106, no. 12, pp. 2246–2257, Dec. 2018.
- [52] W. Bogaerts *et al.*, "Silicon microring resonators," *Laser Photon. Rev.*, vol. 6, no. 1, pp. 47–73, 2012.

Paolo Pintus (S'10–M'11) was born in Cagliari, Italy, in 1983. He received the Bachelor's degree (with Hons.) and the Master's degree (with Hons.) in electronic engineering from the University of Cagliari, Cagliari, Italy, in 2005 and 2007, respectively, and the Ph.D. degree in innovative technologies of information, communication technologies, and robotics from the Scuola Superiore Sant'Anna, Pisa, Italy, in 2012.

From 2012 to 2016, he was a Research Fellow with Scuola Superiore Sant'Anna. He is currently a Project Scientist with the University of California, Santa Barbara, CA, USA. His research interests include integrated optics, silicon photonics, and computational electromagnetics.

Dr. Pintus is a member of the IEEE Photonic Society and the Italian Society for Industrial and Applied Mathematics.

Duanni Huang received the B.S. degree in electrical engineering from the Massachusetts Institute of Technology, Cambridge, MA, USA, in 2013. He received the M.S. degree in electrical engineering from the University of California, Santa Barbara, CA, USA, in 2015, and the Ph.D. degree, in 2019. He was the recipient of an NSF Graduate Research Fellowship in 2015. His current research interests are in the field of silicon photonics, with an emphasis on heterogeneous integration of lasers with isolators.

Paul Adrian Morton received the B.Sc., M.Eng., and Ph.D. degrees in electrical engineering from the University of Bath, U.K., in 1984, 1985, and 1988, respectively. As a researcher with AT&T Bell Laboratories, he made fundamental research contributions in the areas of high-speed laser diodes, mode-locked optical pulse-sources, and photonic integration. He was a technical leader in the development of commercial high capacity DWDM transmission systems with CIENA corporation. In 2002, he co-founded Morton Photonics Inc., West Friendship, MD, USA, a technology company focused on research and development of advanced photonic technologies. He is a founder, C.E.O, and C.T.O. of Morton Photonics Inc., a successful photonic component and sub-systems developer. In recent years, he has focused on developing photonic components, photonic integrated circuits, and subsystems for applications of high performance analog RF Photonic links, sensing, photonic processing for phased array systems, and transitioning these devices to commercial and DoD systems.

Dr. Morton is a Fellow of the Optical Society of America.

Yuya Shoji (M'09) received the B.E., M.E., and Ph.D. degrees in electrical engineering from the Tokyo Institute of Technology, Tokyo, Japan, in 2003, 2005, and 2008, respectively. He was a Postdoctoral Fellow with the National Institute of Advanced Industrial Science and Technology, Tsukuba, Japan, from 2008 to 2010. He has been an Assistant Professor with the Graduate School of Science and Engineering, Tokyo Institute of Technology, from 2011 to 2014. He is currently an Associate Professor with the Laboratory for Future Interdisciplinary Research of Science and Technology (FIRST), Tokyo Institute of Technology. His current research interests include device designs and fabrication of magneto-optical devices, silicon nanophotonic devices, and the photonic integrated circuits.

Dr. Shoji is a member of Optical Society of America, The Institute of Electronics, Information and Communication Engineers, the Japan Society of Applied Physics, and the Magnetic Society of Japan.

Tetsuya Mizumoto (S'81–M'84–F'12) received the bachelor of engineering degree in electrical and electronic engineering in March 1979, the master of engineering degree in physical electronics in March 1981, and the doctor of engineering degree in electrical and electronic engineering in March 1984, all from the Tokyo Institute of Technology (Tokyo Tech), Tokyo, Japan.

He began working with Tokyo Tech in April 1984 as a Research Associate at the Faculty of Engineering and became an Associate Professor in March 1987. He was promoted to a Full Professor with the Graduate School of Engineering in April 2004. From October 2012 to March 2018, he served as the Vice-President for Education with Tokyo Tech and became the Executive Vice-President for Education in April 2018. His research fields are applied optics, photonic circuits, information and communication engineering, waveguide optical devices, especially magneto-optic devices, and all-optical switching devices based on the third-order nonlinearity.

Dr. Mizumoto is a Fellow of Information and Communication Engineers (IEICE), Member of the Japan Society of Applied Physics, and the Magnetic Society of Japan. He was the recipient of the Treatise Award in 1994 and the Best Letter Award of Electronics Society Transactions in 2007 from the Institute of Electronics, and IEICE. He was the recipient the Institute of Electrical and Electronics Engineers (IEEE) Photonics Society Distinguished Lecturer Awards in July 2009, IEEE Fellow grade for "Contributions to investigations of waveguide optical nonreciprocal devices for optical communications" in January 2012, and IEICE Achievement Award for "Pioneering work on optical nonreciprocal circuits" in May 2012.

John E. Bowers received the M.S. and Ph.D. degrees from Stanford University. He worked with AT&T Bell Laboratories and Honeywell before joining University of California, Santa Barbara (UCSB). He is a co-founder of Aurion, Aerius Photonics, and Calient Networks. He holds the Fred Kavli Chair in Nanotechnology, and is the Director of the Institute for Energy Efficiency, and a Professor with the Departments of Electrical and Computer Engineering and Materials at UCSB. He has published 10 book chapters, 600 journal papers, 900 conference papers, and has received 54 patents. His research is primarily in optoelectronics and photonic integrated circuits.

Dr. Bowers is a member of the National Academy of Engineering and a fellow of OSA and the American Physical Society. He is a recipient of the OSA/IEEE Tyndall Award, the OSA Holonyak Prize, the IEEE LEOS William Streifer Award, and the South Coast Business and Technology Entrepreneur of the Year Award. He and coworkers were recipients of the EE Times Annual Creativity in Electronics Award for Most Promising Technology for the heterogeneous silicon laser in 2007.